MASARYKOVA UNIVERZITA
Přírodovědecká fakulta
Ústav teoretické fyziky a astrofyziky

DIPLOMOVÁ PRÁCE

Brno 2023 **Kateřina Svačinková**

MASARYKOVA UNIVERZITA

Přírodovědecká fakulta
Ústav teoretické fyziky a astrofyziky

Charakterizace nerozlíšené emise v Chandra Deep Field-South

Diplomová práce

Kateřina Svačinková

Vedoucí diplomové práce:
prof. Mgr. Norbert Werner, Ph.D.

Brno 2023

Bibliografický záznam

Autor:	Kateřina Svačinková Přírodovědecká fakulta, Masarykova univerzita Ústav teoretické fyziky a astrofyziky
Název práce:	Charakterizace nerozlíšené emise v Chandra Deep Field-South
Studijní program:	Fyzika
Směr:	Astrofyzika
Vedoucí práce:	prof. Mgr. Norbert Werner, Ph.D.
Akademický rok:	2022/2023
Počet stran:	viii + 38
Klíčová slova:	Chandra Deep Field-South, rentgenová spektroskopie, Galaxie, CIAO software, SPEX, Rentgenová observatoř Chandra

Bibliographic record

Author:	Kateřina Svačinková Faculty of Science, Masaryk University Department of Theoretical Physics and Astrophysics
Title of Thesis:	Characterising the unresolved emission in the Chandra Deep Field-South
Degree Programme:	Physics
Field of study:	Astrophysics
Supervisor:	prof. Mgr. Norbert Werner, Ph.D.
Academic Year:	2022/2023
Number of Pages:	viii + 38
Keywords:	Chandra Deep Field-South, X-ray spectroscopy, Galaxy, CIAO software, SPEX, Chandra X-ray observatory

Abstrakt

Chandra Deep Field-South (CDFS) nabízí jedinečný pohled na difúzní rentgenové záření, hlavně v měkkých vlnových délkách. Tepelná emise dominuje této oblasti spektra. Skládá se za prvé z vyzařujícího plazmatu v blízkosti Slunce nazývaného místní horká bublina. Přítomno je také záření pocházející z galaktického hala. Galaktické halo je složitý systém a jeho plazma je v několika teplotních stavech. Konkrétně v horké fázi vyzařující na vlnových délkách rentgenového záření jsou přítomny dvě různé teploty.

Naším cílem je porovnat, jaké rozložení teplot je zodpovědné za měkkou emisi v oblasti Chandra Deep Field-South. Chceme určit, zda je spektrum charakterizováno jednoteplotním, dvouteplotním nebo tříteplotním modelem. Je prezentována analýza spekter ze snímků CDFS získaných dalekohledem Chandra po odstranění všech rozlišených bodových zdrojů.

Zjistili jsme, že třetí teplotní složka představující teplejší fázi cirkumgalaktického média a tepelnou emisi z místní horké bubliny nejsou v našem spektru přítomny. Komponenta místní bubliny pravděpodobně v oblasti CDFS je, ale vzhledem k nedostatečné citlivosti dalekohledu Chandra v oblasti maxima jejího záření však nelze přesně určit její teplotu. Proto lze nerozlišenou emisi měkkého rentgenového záření v našem CDFS spektru popsat jednoteplotním modelem pocházejícím z galaktického hala a mocninnou závislostí extragalaktického původu.

Abstract

Chandra Deep Field-South (CDFS) offers a unique view of diffuse X-ray emission, mainly in the soft X-ray waveband. Thermal emission dominates this region of the spectrum. Firstly, it consists of a radiating plasma near the Sun called the Local Hot Bubble (LHB). Radiation originating from the Galactic halo is also present. The Galactic halo is a complex system, and its plasma is in multiple temperature states. Specifically, two different temperatures are present in the hot phase emitting at X-ray wavelengths.

Our goal is to compare what temperature distribution is responsible for the soft emission in the Chandra Deep Field-South region. We want to determine whether the spectrum is characterized by a one-temperature, two-temperature, or three-temperature model. The analysis of spectra from CDFS images obtained with the Chandra telescope, after removing all resolved point sources, is presented.

We found that the third temperature component representing the hotter phase of the circumgalactic medium and thermal emission from the Local hot bubble are not present in our spectrum. The LHB component is probably in the CDFS region. However, due to the insufficient sensitivity of the Chandra telescope in the region of maximum LHB radiation, its temperature cannot be precisely determined. Therefore, the unresolved soft X-ray emission in our CDFS spectrum can be described by a one-temperature model originating from the Galactic halo and by power law dependence of extragalactic origin.

MUNI
SCI

MASARYKOVA UNIVERZITA
PŘÍRODOVĚDECKÁ FAKULTA
KOTLÁŘSKÁ 2, 611 37 BRNO
IČ: 00216224
DIČ: CZ00216224

ZADÁNÍ DIPLOMOVÉ PRÁCE

Akademický rok: 2022/2023

Ústav:	Ústav teoretické fyziky a astrofyziky
Studentka:	Bc. Kateřina Svačinková
Program:	Fyzika
Specializace:	Astrofyzika

Ředitel *ústavu* PřF MU Vám ve smyslu Studijního a zkušebního řádu MU určuje diplomovou práci s názvem:

Název práce:	Charakterizace nerozlíšené emise v Chandra Deep Field-South
Název práce anglicky:	Characterising the unresolved emission in the Chandra Deep Field-South
Jazyk závěrečné práce:	angličtina

Oficiální zadání:
The Chandra Deep Field-South (CDF-S) is the most intensively studied multi-wavelength deep-survey region across the entire sky. It has been observed by the Chandra X-ray observatory for over 3 months resulting in a unique data set which allows us to study the evolution of galaxies and accreting supermassive black holes, as well as and the X-ray background. The student will process all CDF-S data in the archive in order to gain a deeper understanding of the unresolved X-ray background. After subtracting the instrumental/particle background and removing all resolved sources from this deepest X-ray image ever obtained, the student will characterise the leftover emission from a combination of distant, unresolved accreting back holes and the foreground emission of our Galaxy.

Vedoucí práce:	prof. Mgr. Norbert Werner, Ph.D.
Datum zadání práce:	12. 11. 2020
V Brně dne:	29. 12. 2022

Zadání bylo schváleno prostřednictvím IS MU.

Bc. Kateřina Svačinková, 14. 1. 2021
prof. Mgr. Norbert Werner, Ph.D., 25. 1. 2021
Mgr. Michael Krbek, Ph.D., 1. 2. 2021

Poděkování

Ráda bych touto cestou vyjádřila poděkování svému vedoucímu prof. Mgr. Norbertu Wernerovi, Ph.D. za odborné vedení, trpělivost a všestranou pomoc, kterou mi poskytl při zpracování této práce. Současně bych chtěla poděkovat rodině a svým blízkým přátelům, kteří mi byli podporou po celou dobu mého studia.

Prohlášení

Prohlašuji, že jsem svoji bakalářskou práci vypracovala samostatně pod vedením vedoucího práce s využitím informačních zdrojů, které jsou v práci citovány.

Brno 3. ledna 2023

Podpis autora

Contents

Introduction

The Deep fields have been the subject of studies since 1995 when the Hubble space telescope pictured the Deep Field image. The first image of such kind revealed many galaxies with very low photon flux. Therefore these types of observations became popular in other wavelengths as well. After the Hubble Space Telescope, the Spitzer Space Telescope, Chandra, and the James Webb Telescope also explored the deep measurements, revealing even more information about these sky regions. In this thesis, we will focus on the X-ray mission by Chandra Space Telescope. Chandra began measuring deep fields from its launch in 1999 and kept observing them until 2016. Numerous galaxies and active galactic nuclei were discovered in the X-ray waveband, in both the Chandra Deep field-South and the Chandra Deep field-North, enabling the further study of cosmic X-ray background.

Resolved active galactic nuclei in the studied Chandra Deep Field-South image are interesting, but we can observe the photon flux even after their removal. The weak residual radiation has its source in diffuse emission, consisting of the foreground, representing our Galaxy and the background caused by the cosmic X-ray background. The hard X-ray spectrum well describes unresolved extragalactic detection. Despite that, the soft portion of the X-ray waveband remains mysterious, as the thermal emission originating from the low-density plasma surrounding our Galaxy. Understanding the radiative process in such an environment can provide unique insight into the complex mechanisms in the large envelope, where a massive supply of matter is available, and their properties can shed light on the galactic evolution.

This work is divided into four chapters. In Chapter 1, we deal with an overview of the processes that can occur in the CDFS region. Data preparation and processing is discussed in Chapter 2. The results of the work are presented in Chapter 3 which are subsequently discussed in Chapter 4. The conclusion is raised in Chapter 5.

Chapter 1

Theoretical part

1.1 Active galactic nuclei

Since the discovery of Active Galactic Nuclei (AGNs) Seyfert (1943), an enormous number of AGNs have been detected. AGNs are a matter of great interest, and large telescope missions allow us to study their physical properties, evolution, or how they react to the environment.

AGN is a compact region located at the centre of specific galaxies, whose source of brightness is the accretion disk around the supermassive black hole (SMBH). The mass from the accretion disk falls into the black hole, and thanks to this powerful process, the AGNs attain enormous brightness. [E01]

Many types of AGNs, such as Quasars, Blazars, Seyfert galaxies, and Radio galaxies, have various phenomenological and spectral features across all wavelengths. Quasars radiate at all wavelengths. Their flux is variable in all parts of the spectrum, where the time-scale of this variability depends on the wavelength and the type of specific object. Quasars are objects that outshine their host galaxy and maintain a luminosity range from 10^{45} to 10^{49} erg s^{-1}. Its continuum spectrum can be described by power law over broadband frequencies, from radio to hard X-ray. (Schneider, 2015)(Rosswog and Brüggen, 2007)

Radio galaxies seem to be regular elliptical galaxies but have an AGN in the centre and emit an extreme amount of radiation in the radio wavelength. Luminosity reach up to 10^{41} erg s^{-1}. big radio lobes that stretch up to several kiloparsecs are most likely the source of this radio emission. Radio galaxies can be divided into Fanaroff-Riley type I (FRI), in which case the source is brightest near the centre, and to Fanaroff-Riley type II (FRII), with powerful jets and so-called hot spots farther from the centre. (Rosswog and Brüggen, 2007)

Another type of AGN are the Seyfert galaxies, which can be distinguished, based on their spectra, as the Seyfert galaxy 1 and the Seyfert galaxy 2. Type 2 shows signs of permitted and forbidden lines from the narrow-line region, and type 1 displays additionally the permitted lines from the broad-line region. (Antonucci, 1993)

The most luminous of all AGNs are probably Blazars. They display high optical polarization and intense X-ray and Gamma-ray luminosities. Blazars are also highly variable, with a typical spectrum corresponding to synchrotron

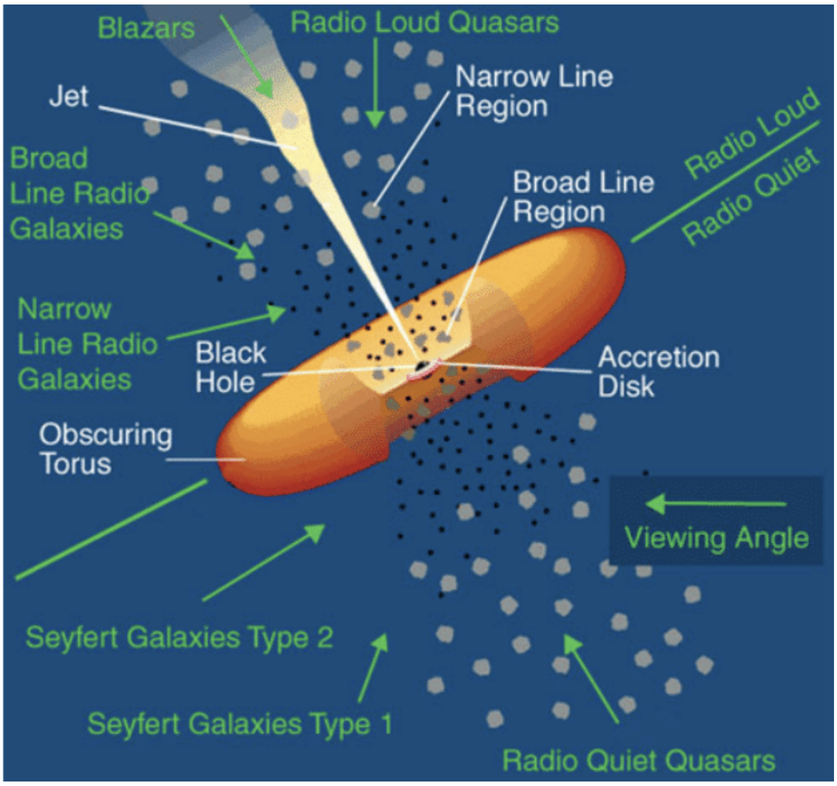

Figure 1.1 Illustration of an AGN.(Schneider, 2015)

radiation. Superluminal motion seems to occur at this type of object, causing the components of the source observed to have a speed greater than the speed of light, which is just an optical illusion. (Rosswog and Brüggen, 2007) (Longair, 2011)

Unified models

Antonucci (1993) mentioned that all these species probably have similar physical properties but differ in orientation relative to the line of sight, and he defined the so-called Unified model. In the Unified model, he defines two basic types of AGNs, radio-quiet and radio-loud objects. The radio-quiet AGNs include Seyfert galaxies types 1 and 2. Radio-quiet objects are a type of AGN that is not accompanied by a strong jet emitting in the radio waveband.

The optical properties of radio-loud galaxies are almost the same as those of radio-quiet objects. Radio-loud objects can be divided into FR1s, with weak, narrow emission lines and no broad lines. On the contrary, FR2 AGNs have strong narrow lines or broad lines and a featureless continuum. In contrast to Radio-Quiet AGNs, radio-loud objects are usually associated with powerful jets. (Antonucci, 1993)

As already mentioned, the specific type of object depends on the orientation of the AGN. Figure1.1 is a good demonstration of how the AGN and its types depend on the angle of view.

1.1.1 X-ray emission from Active Galactic Nuclei

X-ray radiation is a probe to the innermost part of the AGN. In Figure 1.2, we can see a scheme of the typical AGN X-ray spectrum. The spectrum extends from ~ 0.1 keV up to ~ 100 keV and is composed of multiple components. The combination of these segments is a consequence of the processes by which X-rays originate in the environment around SMBH. The exact model is not known yet. It is believed that the alleged corona is responsible for the X-rays. This corona is in the form of hot plasma above the black hole and the accretion disk, which then irradiates the disk. To a first approximation, the X-ray spectrum of an AGN is characterized by a power law. For radio-quiet objects, the steeper slope of the function is typical, while a flattener slope is common for radio-loud objects. The power-law spectrum is created by inverse Compton scattering of thermal photons in the corona. The slope of the spectrum depends on the corona's temperature and the optical depth. (Schneider, 2015) (Dovciak, 2004)

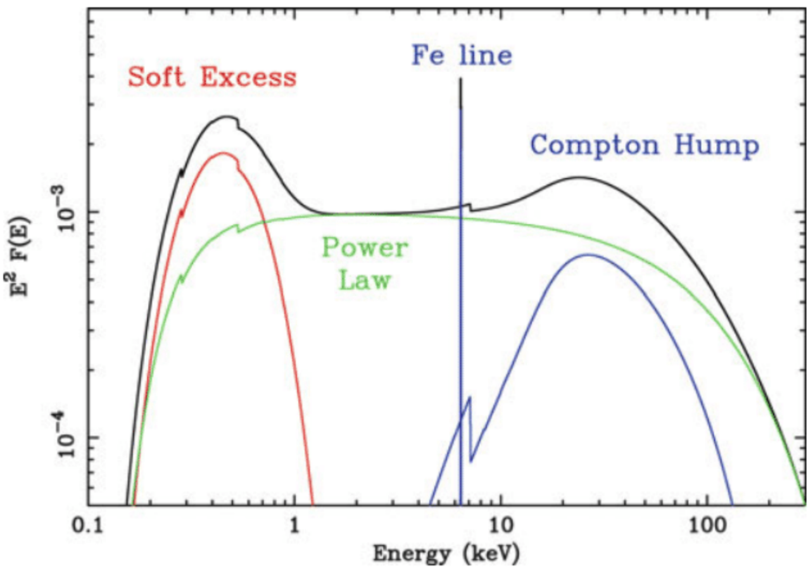

Figure 1.2 Scheme of the typical X-ray spectrum of the AGN (Schneider, 2015).

There is a slightly different characteristic at lower energies (close to the lower limit) than the power-law dependence. This deviance is called soft excess. Thermal emission is responsible for this excess, and it is most common in objects where the temperatures of the accretion disk are much higher, and the black body emission extends to soft X-ray energies. (Dovciak, 2004)

Another discrepancy, called the Compton hump, is present at higher energies. The reason behind this is a reflection on the accretion disk. The photons from the corona can also hit the original disk, and they can be, in the case of lower energies absorbed, or they can be scattered inside the disk if their energy is high enough. (Schneider, 2015)

Characteristic line emission is also present in the spectrum. Line emission is comparable to the previous case caused by the corona's illumination of the accretion disk. In this case, fluorescence occurs when high-energy corona photons hit atoms in the disk. The strongest line is the iron line at 6.4 keV. (Schneider, 2015)

1.2 Galactic halo

Our Galaxy is a spiral type consisting of several components. Although the Galactic system may appear relatively simple, especially in the visible part of the spectrum, it is composed of very complex processes.

The main part of spiral galaxies is the disk, consisting mainly of stars and the interstellar medium. The galaxy is also formed by the bulge, in which the SMBH is located. The bulge represents roughly 20% of the galactic stellar mass, while the stellar disk occupies up to 80%. Apart from these components, the galactic halo is also part of the system, making up about 1% of the total mass. There is a halo formed by dark matter and a stellar halo formed by stars, either bound in globular star clusters or moving independently. An addition is then the circumgalactic medium (CGM). This medium is the gas located outside the stellar disk, extending to a distance reaching the maximum value of the virial radius. The CGM has complex dynamics and is very important for understanding galaxy evolution, but because it is so dimly visible, it is not yet fully understood.

Many previous observations focused on both the CGM of our Galaxy and the atmospheres of galaxies similar to the Milky Way. These observations have shown a wide range of different ionized material states in these media and, thus, a large range of gas temperatures and densities with varying kinematic properties.(Fielding et al., 2020)

1.2.1 Structure of the circumgalactic medium

The cold gas found in the CGM is one with temperature $< 10^4$ K. It most likely originates from the warm gas, which gradually cooled to the phase of cold material, thanks to the thermally unstable environment. Cold gas consists mainly of neutral H, Ca, and Na atoms or weakly ionized atoms of these elements. The low-temperature material occurs in the form of clouds and is closer to the Galactic disk (up to 20 kpc) than the warmer material. Putman et al. (2012) determined the total mass of cool gas in the CGM to be approximately 10^7 $M_\odot$. Material from the Magellanic Stream is not counted as part of the cold gas because this matter cannot be considered a standard part of the galactic system. (Tumlinson et al., 2017)

Another material phase is the cool gas with temperatures $\sim 10^{4-5}$ K. At this range, a strong line absorption in the ultraviolet spectral region occurs. This makes the cool gas the most understood phase. The cool part of the CGM was investigated in low redshift galaxies and is composed of additional doubly or triply ionized C, Si, and N atoms. It was modeled based on observations of galaxies with luminosities similar to luminosity of our Galaxy $L \approx L^*$, and the cool material mass was estimated as $M_{cool} = 6.5 \times 10^{10}$ $\mathrm{M}_\odot$. The warm CGM with temperatures of $\sim 10^{5-6}$ K appears similarly to cold material by absorption lines in UV light. Unlike the cold material, we can observe higher degrees of ionization, mainly for C, N, O, and Ne atoms. However, this part of the CGM can blend with the emission from ions in a cooler environment. Therefore the measurement in this area is burdened with uncertainty. In the case of our Galaxy, cold and warm material is detected by H_α emission and ion absorption lines. The mass of this material is $3 - 4 \times 10^7$ $\mathrm{M}_\odot$, but this value may vary, as part of this mass may have already been accounted for in the previous cold phase. (Tumlinson et al., 2017) (Putman et al., 2012)

The hot phase with temperatures $> 10^6$ K differs from the previous ones, as its density is low and difficult to detect. This hot gaseous halo is in a state with virial temperature T_{vir} and extends to the distance with virial radius R_{vir}. According to the virial theorem, the kinetic energy E_k of the particles in the gas balances the negative potential energy E_p of these particles, i.e. $2E_k = -E_p$. The kinetic energy of the gas in the galactic halo is equal to the thermal energy, that is

$$E_k = \frac{3}{2}\frac{k_B T}{\mu m_p}, \tag{1.1}$$

where T is temperature, μ is weight for particles in ionized gas, k_b is Boltzman constant and m_p is mass of a proton. Potential energy is then

$$E_p = -\frac{GM}{R}, \tag{1.2}$$

where G is the gravitational constant, M is the mass of the gas, in our case corresponding to the mass of the gaseous galactic halo and R is the radius equal to the virial radius. According to the virial theorem, then

$$\frac{kT}{m_p} = \frac{GM_{halo}}{R_{vir}}, \tag{1.3}$$

and the virial temperature of the gas in the hot galactic halo is

$$T_{vir} = \frac{GM_{halo} m_p}{kR_{vir}}. \tag{1.4}$$

Such a hot environment appears mainly through X-ray radiation, but the emitting light can also extend into the extreme UV region. Since the gas in the hot halo is difficult to detect, the exact determination of its parameters, such as the total mass, is difficult. As the mass of this material is not determined precisely enough, it is speculated that the so far undetected gas in the CGM could solve the problem of missing baryons. However, calculations still show that this gas could occupy only 6-13% of the total mass of the missing baryons. The hot Galactic halo extends to great distances, and the dwarf galaxies that orbit the Milky Way, including the Magellanic Clouds, are embedded in this hot medium, which likely affects their interaction with our Galaxy. The hot CGM also interweaves clouds of low-temperature media, as the material in all the mentioned phases interacts with each other and is subject to complex, yet not fully understood, dynamics. (Fielding et al., 2020), (Putman et al., 2012), (Lochhaas et al., 2021)

1.2.2 Kinematics and dynamics of the circumgalactic medium

Several processes could lead to the creation of such a complex and extended system, located in several phases. Inward cooling flows driven by local thermal instability could be responsible, as well as boundary layers between clouds in the cold phase and gas from the hot halo or continuous shocking and mixing of gas by the galactic outflow. Observations of galaxies similar to ours have shown several phenomena, including outflows and recycling of matter. Based on these observations, the more ionized the gas, the greater its turbulent velocity, usually from 20 km/s for areas with a lower degree of ionization up to 50-75 km/s for matter in a higher ionization state. Observations are, however, very limited by the blending of lines, and more precise instruments would be needed to determine the movement of the medium better. Cosmological hydrodynamic simulations can help to understand why this mixed medium was formed and maintained in its current state. The simulations can analyze the relationship of the multiphase medium to the dark matter halo or accretion initiated by gas from the galactic disk ejected by the so-called galactic fountain. (Tumlinson et al., 2017)

A sketch of the flow mechanism likely to occur in our Galaxy system can be seen in Figure 1.3. It is generally believed that gas flowing from the intergalactic medium (IGM) is accelerated into the galactic disk, creating an inflow. On the other hand, the source of the outflow is material created in supernova explosions or during star formation. These two types of currents should then be balanced so that the mass exchange system remains in equilibrium. If the matter flow falling on the galactic disk were not balanced with the galaxy-originating streams, there would not be enough material left to form new stars. However, this model does not consider the presence of the CGM, through which the IGM should pass. Thus, gas in the galactic halo could play a role in regulating star formation in galaxies. (Tumlinson et al., 2017)

The gas in the CGM that would eventually fall on the galactic disk is in an ionized state, and on its way, it would have to pass through the HI hydrogen layer. These factors would then appear in the star formation and thus in the interstellar medium (ISM). During observations of nearby galaxies, Ly_α absorption lines were observed in their halos and were shown to be consistent with HI properties in the ISM. Specifically, it was a connection between the equivalent width of the Ly_α lines and the mass of ionized hydrogen in the disk. However, there was also a correlation between equivalent widths and the star-forming rate. This is

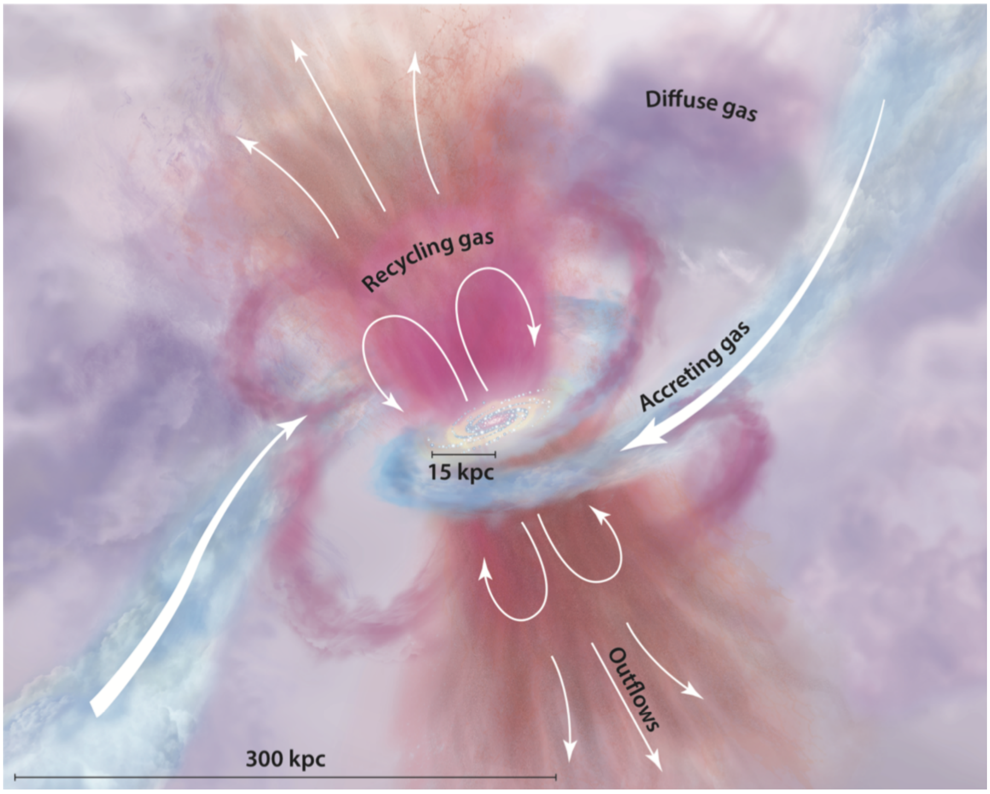

Figure 1.3 A sketch representing the accretion system of the galaxy. Cool and cold gas is represented in blue colors. Outflow gas with warmer temperatures is shown in orange/pink colors. Hot diffuse gas is then represented by purple. (Tumlinson et al., 2017).

evidence of currents and exchanges of material between the atmosphere of the galaxy and its disk. In the case of the Milky Way, we can observe more clear evidence of outflows and inflows, which is the Doppler shift of moving clouds in the CGM. (Borthakur et al., 2015)

The presence of the matter accelerating into the disk and the outflows from the galaxy could indicate the existence of galactic recycling. Thus, the gas carried out of the galactic disk cools down again in the halo and falls back. Cosmological simulations support this recycling to explain the processes observed in the nearby galaxies. However, a detailed description using simulations is limited by the lack of information about what drives these flow mechanisms. After matter accumulates and causes new star formation, the environment reacts by ejecting material and radiation, which then heats and ionizes the medium outside the galactic disk. This happens through supernova explosions, central black hole feedback, winds driven by the radiation momentum, or galactic fountain. The fact that the hot CGM reaches the limits of the virial radius also indicates the presence of currents originating from the galaxy's interior, existing in different velocity ranges. Material with a higher velocity then leaves the system in contrast to the low-velocity medium that feeds the hot halo. (Tumlinson et al., 2017) (Putman et al., 2012)

In addition to the feedback flows already described, the CGM is also powered by material from the IGM and particle inflow from satellite dwarf galaxies. The gas from the filament can accelerate either in the so-called hot mode or through shocks at the virial radius. Nevertheless, it can also accelerate via the cold mode ($T \lesssim 10^{5.5}$ K), which is not, in contrast to the previous case, accompanied by the shocks. The material moving from the filament then merges mainly with the hot galactic halo, which could also explain why we observe hot gas at such great distances. Mostly, the ongoing accretion is in hot mode when the gas heats, thanks to the occurring shocks. This material inflow is not directly connected to the galactic disk but reaches the disk regions only after mixing with the CGM. (Putman et al., 2012)

1.3 Diffuse X-ray Emission

Diffuse X-ray emission is radiation not confined or localized into resolved or point sources. Examples of diffuse emission include light from gas and dust, stellar-connected outflows, radiation related to the magnetic field, or extragalactic emission.

Below 1 keV, Galactic emission dominates, consisting mainly of the Local Hot Bubble (LHB) and the Galactic halo components. A large contribution to the Diffuse X-ray background comes from unresolved point sources. These objects are not bright enough to be differentiated as individual sources. Objects like AGNs, star-forming galaxies, galaxy clusters, or even stars can contribute, dominating the spectrum above 1 keV with a characteristic power-law shape. (Galeazzi et al., 2009)

1.3.1 Physics of hot plasma

A vast part of the diffuse emission consists of radiation emerging in the hot plasma environment. Specifically, it is the soft part of the X-ray spectrum up to 1-1.5 keV.

The ionization of neutral gas creates plasma. Firstly, neutral gas has a lower temperature, receives kinetic energy, and heats up. Once it gains enough heat, the thermal energy begins to overcome the binding energy, and the particles in the gas dissociate. Higher excited states gradually increase until, in the end, an ionized plasma is formed. The material in the medium is classified as plasma if the total charge of the contained particles is in equilibrium, i.e. $n_e = \sum n_i$, where n_e is the concentration of electrons and n_i is the concentration of ions. Debye length is defined as

$$\lambda_D = \sqrt{\frac{\epsilon_0 k_B T}{ne^2}}, \tag{1.5}$$

where ϵ_0 is the vacuum permittivity, e is the charge and n is the concentration. The previous condition does not apply only on scales smaller than the Debye length λ_D, i.e. if the system is much larger than the Debye length, the material can be categorized as a plasma. To talk about plasma, $n\lambda_D^3 \gg 1$ must also be in effect, i.e. the mean distance between electrons must be small compared to the Debye length. (Bittencourt, 2013)

Collisions play an essential role in the plasma, as they contribute to the overall equilibrium of the system. In astrophysical environments, collisionless plasma is mainly found since its density is very small and the mean free path of the particles is large. Therefore collisions occur less often. As it is a diffuse plasma, it emerges when a density gradient is present. Both ions and electrons then move to places with lower density. For example, the density of hot plasma in the hot galactic halo of our Galaxy is approximately 10^{-5} and 10^{-4} cm^{-2} at $50 - 100$ kpc. (Putman et al., 2012) (Bittencourt, 2013) (Fitzpatrick, 2022)

Although in the case of a hot galactic halo, where a very thin plasma is present, frequent collisions do not occur, the plasma has very high temperatures and, thus, a high degree of ionization. Therefore, mainly line emission appears due to excitation and recombination. (Bittencourt, 2013)

1.3.2 Obscured active galactic nuclei

Outside the limit of 1.5 keV in the X-ray spectrum, there is almost no emission from hot gaseous material, e.g. from the CGM in our Galaxy. In these areas, it is mostly radiation from extragalactic sources. Specifically, the emission from AGNs, which are either very distant or heavily obscured, cannot be resolved as point sources.

The question of whether an AGN is obscured or not depends on the angle from which we look at the SMBH. Figure 1.4 shows the dependency on the line of sight. More factors can influence the detected signal, as the torus properties can also play a role.

If the jets of a black hole point perpendicularly to Earth or at angles close to 90°, we are looking directly into the dust and gas torus surrounding the black hole and its accretion disk. The torus captures most of the photons coming out of the SMBH, and they do not reach us to such an extent.

The material that blocks the light from a black hole is typically in the form of dust and gas. However, the torus that lies between us and the black hole is located near the accretion disk and is still under the influence of the SMBH. Unlike AGN showing no signs of obscuration, narrow line region (NLR) lines can be detected in the spectra of obscured AGN. These lines are not blocked by obscuring material, in contrast to the broad line region (BLR), the absence of which can define obscured AGN. BLR and NLR are observable in optical wavelengths. If we want to talk about X-ray radiation, it is closely related to the accretion disk. It originates explicitly in the region of the so-called corona, as was already discussed in Chapter 1. For photons coming from AGN, it is generally true that those with lower energy are more easily absorbed than photons with

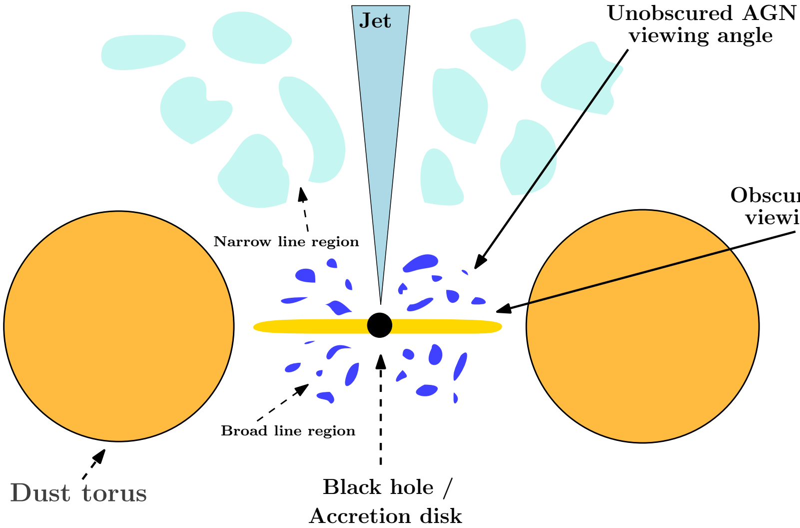

Figure 1.4 A sketch of AGN, picturing the difference between obscure and unobscured viewing angle.

higher energy. Hence the emission from obscured AGN is most likely to be detected in the hard part of the spectrum. (Hickox and Alexander, 2018)

The X-ray surveys taken so far show that the majority of AGNs in the Universe are obscured. It was also found that the fraction of obscured AGNs decreases with increasing X-ray luminosity, most likely because strongly emitting black holes can scatter or destroy their enveloping disks due to radiative feedback. Another important finding brought by the X-ray survey is a dependence of the ratio of obscured AGNs on the redshift z in which the given galaxy is located. This dependence can be described using the formula $(1+z)^{0.4-0.6}$ up to the distance where $z \approx 2$, then large uncertainties occur, and the dependence cannot be determined precisely. This relation could be explained by the availability of gas and dust in galaxies during the early cosmic times. (Brandt and Alexander, 2015).

1.3.3 Hot circumgalactic medium

The details of the CGM were already discussed in Section 1.2. Here we will take a closer look at the hot part of the Galactic halo and its structure and properties. As already mentioned, the hot plasma surrounding the Galactic disk extends up to the virial distance (~ 250 kpc) and possibly beyond. The material in this part of CGM is very hot and has low densities. Because of this, it is not possible to determine exactly how much mass is in it (the estimate is $10^{10} - 10^{11}$ $M_\odot$). Hot CGM means temperatures of $\sim 10^6$ K, but a component with higher temperature was recently discovered, namely $> 10^7$ K, indicating that even a hot phase consists of several parts.

Hot CGM has been the subject of several studies. It can be observed from both emission and absorption X-ray spectra. Another method for its observation is the detection of high-velocity clouds (HVC). The clouds are moving at speeds greater than the typical Galactic rotation speed and have been observed outside the Galactic disk. The problem is that these clouds should have evaporated before reaching their observed velocity. This problem could be explained if the cooler, fast-moving clouds were enveloped by hot gas, preventing the escape of cool material. The clouds could reach higher speeds then due to longer lifetimes. The shape of HVC also corresponds to the fact that they move across a hotter medium. (Bluem et al., 2022)

Something must have caused the gas to be at such high temperatures. Processes inside the Galactic disk are responsible for both the ionization and heating of the plasma. Namely, it concerns supernovae and feedback from the Galactic core. Also, the presence of metals in the CGM indicates a contribution from the Galactic disk since the intergalactic medium is only slightly rich in metals. It is also likely that the structure of the hot medium present in the Galactic halo is not homogeneous but shows clumpiness, as it shows changes on the angular scale. (Bluem et al., 2022)

1.3.4 Local Hot Bubble

The Sun is, inside the Galactic plane, surrounded by plasma. This plasma material has a different density and temperature than the average material in the interstellar medium of our Galaxy. The temperature of the material has a high value, therefore, it is called the LHB. A model of the LHB can be seen in Figure 1.5. Since the temperatures in this cavity are high ($\sim 10^6$ K), it emits radiation in the soft X-ray region and appears as a background while observing various X-ray objects. (Pelgrims et al., 2020)

Around this plasma bubble, a layer of cold, neutral gas and dust exists. Only recently, the shape and extent of the LHB were discovered. Recent research based on data from the Gaia satellite has shown new results. The motions of gas clouds and stars in the region within 200 pc of the Sun were investigated. Based on calculations, the fact that all new star-forming regions close to the Sun lie on the surface of the LHB was revealed. The young stars in these regions exhibit motion away from the Sun, perpendicular to the surface of this bubble. (Zucker et al., 2022)

As for the evolution of the LHB, it was clear that its formation is somehow connected with supernova explosions. Clarification was provided only by discovering moving groups of young stars near the Sun. During their passage through the LHB region, these groups could have provided sufficient supernovae to fill

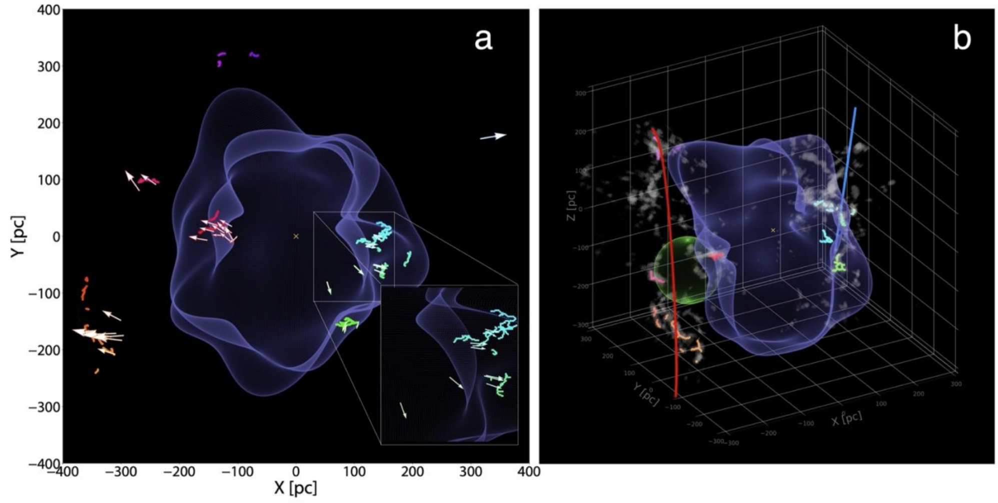

Figure 1.5 A top-down projection can be seen in panel a. In panel b, a 3D view of the relationship between the LHB, nearby star-forming regions, and the Galactic structure is shown. A 3D model of the LHB (purple). The Sun is placed in the centre of the images (yellow cross). Star-forming regions are also displayed, as well as young stellar clusters (arrows). (Zucker et al., 2022)

the local cavity with hot gas. An example is the trajectory of a moving star group, whose remains are now part of the Scorpio Centaurus OB association. Using the trajectories of the group stars, it was shown that 19 explosions possibly occurred in the LHB space around 10-20 Myr ago. Other young stellar associations were examined similarly. Based on these calculations, the age of the LHB was determined to be between 10 and 15 Myr, with 14-20 supernova explosions present, filling the region with high-energy particles in the form of hot plasma. (Fuchs et al., 2006)

1.3.5 Other contributions to Diffuse X-ray background

One of the other contributors is the solar wind charge exchange (SWCX), during which high-velocity solar wind ions collide with low-motion particles inside Earth's magnetosphere, creating X-rays photons. During the collision, the ions give one of their electrons to the target atom. Subsequently, the electron decays with simultaneous X-ray emission. Such a process is useful for understanding solar wind and Earth's magnetosphere. However, it can be problematic when studying the Galactic halo or LHB as it contaminates the data and is hard to subtract. It is believed that SWCX X-rays are contributing to X-rays attributed to the LHB inside the Galactic plane. How much the SWCX X-ray photons contribute to the LHB emission is still a matter of debate. (Kuntz, 2019)

Solar wind charge exchange is also present in datasets with Galactic halo spectra. In this case, it is much easier to consider the contamination. The shadowing method is used for these cases as was done by Henley and Shelton

(2015). This method uses a cloud with known column density. The spectrum is then measured "on-cloud" and "off-cloud", and after, the background and foreground emissions can be resolved. As the origin of this process is in the solar wind, it is mostly observed in the Galactic plane. Because the CDFS region is located outside the Galactic plane, we do not deal with SWCX contamination in this thesis. (Kuntz, 2019)

Another emission that can be detected has a source in the hot filament, connecting the Local group of galaxies, the Warm-Hot Intergalactic Medium (WHIM). The material in the filament has a low density and T of $\sim 5{\times}10^5$ K. Therefore, the matter is in a state of highly ionized plasma and is visible in soft X-ray and UV light. The flux from the WHIM is very weak, overshadowed by sources from our Galaxy and unresolved point sources. Therefore it cannot be observed in our set of data. (Galeazzi et al., 2009) We can see all the possible contributions to the diffuse background in Figure 1.6.

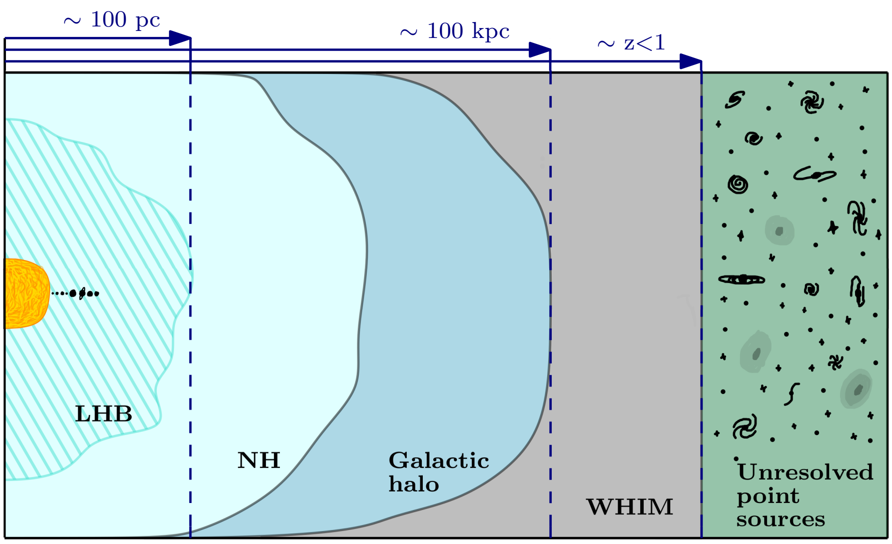

Figure 1.6 An illustration of diffuse X-ray background.

1.4 Chandra Deep Field-South

Deep surveys can be a good source for researching distant objects at all wavelengths, as objects of the same type emit less at larger distances and, therefore, in early times. Each region of the deep field spectrum can tell us something different. The X-ray region gives us an insight into very energetic processes in the Universe.

The most important surveys in the X-ray waveband are Chandra Deep Field-South with ≈ 7 Ms exposure taken with Chandra X-ray observatory. Similarly, Chandra Deep Field-North with exposure of ≈ 2 Ms. Both regions were chosen near the Galactic poles to be far from any strong X-ray sources. As for the CDFS, it is located near the south Galactic pole, and it occupies a total area of 484.2 arcmin^2 with the centre lying at the coordinates RA 3h 32m 28.0s DEC -27°48'30" (J2000.0). The area's location in the context of the all-sky survey can be seen in Figure 1.7. (Luo et al., 2017) (Sharma et al., 2022)

Many types of objects are observed in the CDFS image, most of which are AGNs. Specifically, unobscured AGNs, obscured AGNs, and optically faint X-ray sources are probably also AGNs but cannot be confirmed spectroscopically. However, so-called X-ray bright, optically normal galaxies are also present. They are early-type galaxies that show weak signs of core activity but appear normal in the optical waveband. In addition to AGN, other objects are also present: starburst and normal galaxies, groups and clusters of galaxies and galactic stars. The stars are members of our Galaxy, located inside the area of the deep field region. (Brandt and Hasinger, 2005)

The most detailed analysis of objects in the CDFS was performed by (Luo et al., 2017), who created the most up-to-date catalogue of the sources. They found 1008 objects in the CDFS region with a median z = 1.12 ± 0.05. Of the discovered objects, 711 were characterized as AGNs, 12 as stars, and the remaining 285 were probably normal galaxies.

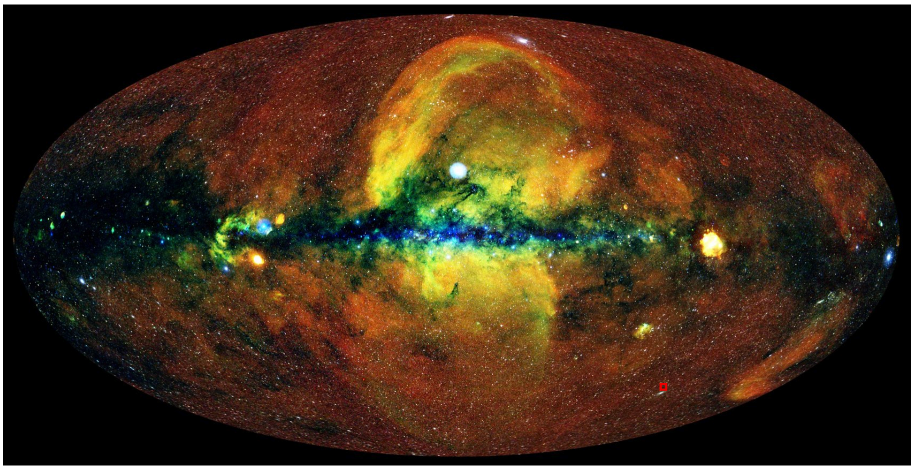

Figure 1.7 The eROSITA all-sky survey in 0.3-2.3 keV band [E02], with CDFS location (red square).

Chapter 2

Data analysis

2.1 Chandra X-ray Observatory

Chandra is an X-ray detecting space telescope launched on July 23, 1999. The most important part of the telescope system is the High-resolution Mirror Assembly (HRMA), consisting of four concentric grazing incident X-ray telescopes, focusing X-rays on the selected detector in the Science Instrument Module(SIM). Part of the SIM are two focal plane instruments, an advanced charged coupled device (CCD) Imaging Spectrometer (ACIS) and High-Resolution Camera (HRC). ACIS is an array of CCDs that can simultaneously obtain high-resolution images and moderate resolution spectra. It consists of 10 planar 1024x1024 CCDs. Four are arranged in a 2x2 array (ASIC-I), used for imaging, and six are arranged in a 1x6 array (ASIC-S), used either for imaging or grating spectrum read-out. ACIS CCDs configuration can be seen in Figure 2.1. [E03]

Princip of the ACIS array is based on the photoelectric absorption of an X-ray photon in silicon. Such an event results in freeing a proportional number of electrons. After photoelectric absorption, the charge is confined by an electric field. A typical ACIS operation looks like this. Firstly the active region is exposed for a fixed amount of time. Then at the end of exposure, the charge in the active region is quickly transferred in parallel into the frame store. After, the next exposure begins and simultaneously, the data in the frame store region are transferred serially to a local processor, which identifies the position and amount of charge collected.[E04]

On the focal plane is another instrument, the microchannel plate called HRC. The HRC is composed of two components. One optimized for imaging (HRC-I) and one read-out for Low Energy Transmission Grating. In contrast to ACIS, HRC-I possesses a large field of view, and its response also extends to energies below the sensitivity of ACIS. The HRC instrument has a UV/Ion shield to filter signals from UV light, ions and low-energy electrons. X-ray light first goes through this shield. After, photons are absorbed in the CsI-coated walls of MCP. CsI coating is present because it enhances photoemission. An electric field then accelerates photoelectrons. Subsequently, secondary electrons are released due to interaction with MCP. This goes on until a cascade of electrons is produced. An electron cloud that is accelerated towards a charge detector is created from

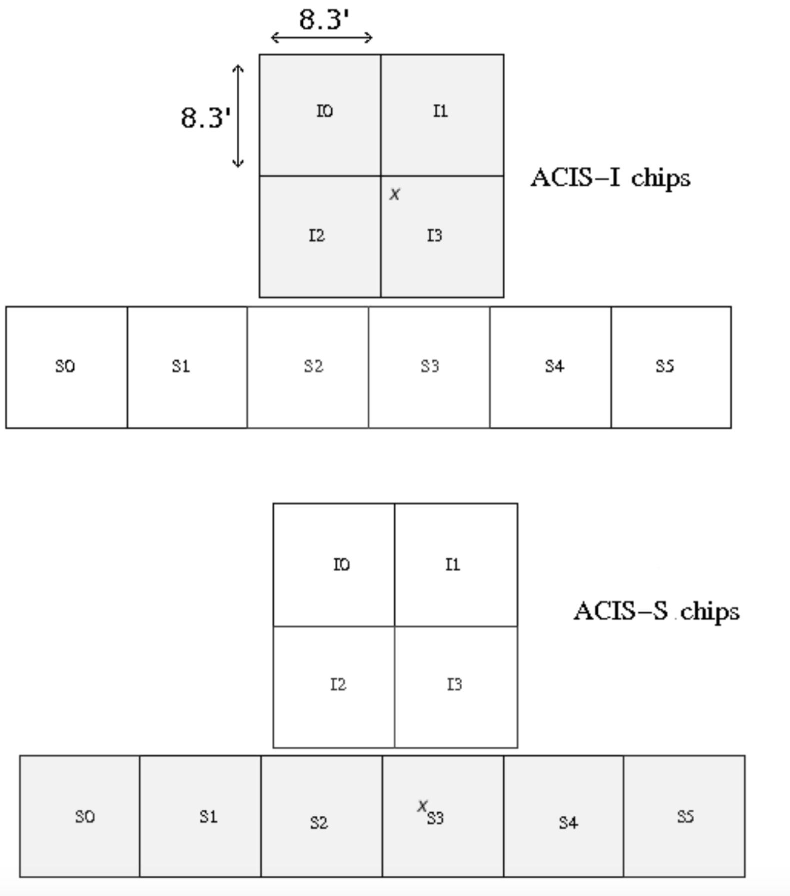

Figure 2.1 A schematic drawing of ACIS focal plane. The ACIS-I array consists of chips I0-I3 (shaded gray in the upper figure). The ACIS-S array consists of chips S0-S5 (shaded gray in the lower figure). [E04]

the cascade. X-ray position is then determined by calculating the centroid of the charge cloud. [E05]

2.2 Data preparation

We analyzed a total of 109 observations of Chandra Deep Field-South taken by the Chandra X-ray telescope between 2000 and 2016. The Chandra telescope observed CDFS for a total exposure of $\sim$ 7 Ms. Nevertheless, due to data filtering and specific region selection, part of the total exposure was lost during the preparation process. All the observations were taken with ACIS-I chips, as they are better suited for diffuse background measurements than ACIS-S chips.

Two telemetry modes were used in the CDFS dataset. The observations measured during the year 2000 were taken in Faint mode (F), as the Very Faint (VF) telemetry mode was initiated after the year 2000. Introducing VF mode helped distinguish between good X-ray photons and bad events most likely associated with cosmic rays. [E06]

The CIAO: Chandra Interactive Analysis of Observations software package (Fruscione et al., 2006), was used for processing the data. The Chandra X-ray Centre developed the CIAO specifically for analyzing data from the Chandra space telescope. Version 4.14 of the CIAO software package was used.

The observations were firstly downloaded using the `download_chandra_obsid` command, which downloads observations from the public archive based on their IDs. All the observations were then reprocessed by `chandra_repro` command. During the reprocessing, CIAO uses primary and secondary data downloaded via the method mentioned in the previous step and calibrates them to be compatible with steps in further analysis. The additional reprocessing parameter, the `check_vf_pha`, was set to 'no' in the case of an F mode and 'yes' when the VF mode was set up. When the parameter is fixed to 'yes', the script cleans the ACIS particle background of unwanted events and helps reduce the data noise.

2.2.1 Removing Background flares

Robust features present in the light curves of the observations, called flares, are part of an ACIS CCDs background. They are usually highly variable on timescales of seconds to hours. The flares are created by charged particle contamination when secondary particles scattered by the telescope walls have enough momentum to be undiverted by the magnets and land on the detector plane. They are probably connected with solar weather as more charged particles hit the telescope during solar events. An example of such a flare can be seen in Figure 2.2.

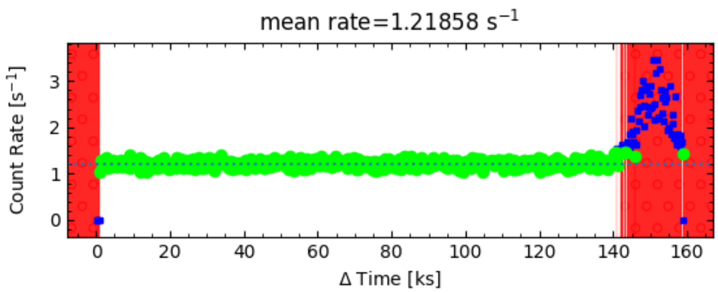

Figure 2.2 An example of light curve contamination by a flare.

Several important steps needed to be taken to eliminate the flares captured during our measurements. Firstly, the light curves were obtained applying `dmextract` script on the reprocessed event FITS files. The features in the light curves were then identified with `deflare` routine. As Python routine, deflaring will remove flares as well as periods with anomalously low count rates. After, the mean count rate is determined using the Poisson statistic with subsequent sigma value calculation. The counts outside the three-sigma interval are then removed from the light curves. In Figure 2.3, examples of no and strong flaring present can be seen. The counts outside the selected sigma interval are pictured in red colour. These counts are removed from observations. [E07]

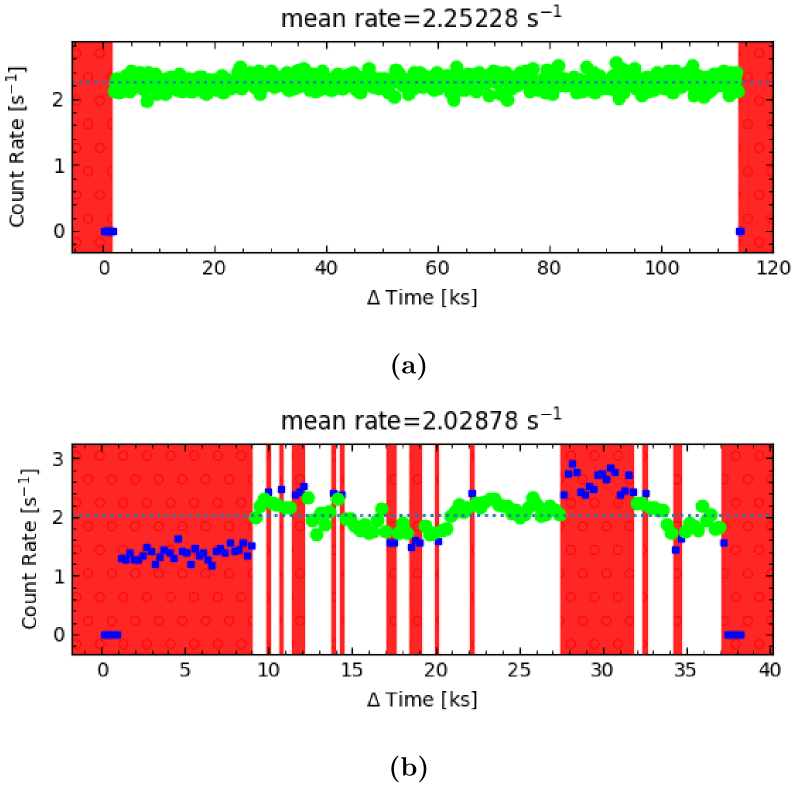

Figure 2.3 The light curves of the CDFS observations. In a), an example of observation without any background flaring is displayed (ID 12052). Observation, with very strong flaring, is plotted in b)(ID 17633).

Because of the intense flares, observations with IDs 581,16184, and 17633 were discarded from the analysis.

2.2.2 Quiescent background

The quiescent background is relatively constant in time than the background flares. The Chandra telescope takes multiple background images to remove instrumental particle background, such as dark Moon, blank sky and stowed background observations.

The telescope was pointed on the dark Moon in July and September 2001 to distinguish the Cosmic X-ray Background from the instrumental background component. It was determined that the dark Moon measurements are insufficient as they do not deal with emission originating within the Solar system. The fact that the Chandra aspect camera cannot be used near Moon also adds to the problem of using dark Moon observations. In addition, this background can be applied only on S chips, as the I chips are not designed to filter light reflected from the Moon. (Markevitch et al., 2003)

Blank-sky images can serve as a suitable replacement for background measurement. They were created when the telescope was pointed at an empty part of the sky. Unlike the dark Moon measurements, blank-sky images are adequate for analysis, where sensitivity in the soft X-ray band is unnecessary. As our data set has low flux and our analysis is most important in the lower energies, the background needs to be subtracted as precisely as possible. Therefore the blank-sky images are not good enough, as the valuable data in the soft band would be lost.

For the reasons listed above, stowed background images are used in our analysis. Stowed background observations were measured when the CCD chips were stowed inside the detector's housing. Such telescope setup allows the background not to be affected by any effects other than instrumental background. The comparison of the blank sky and stowed background images is shown in Figure 2.4.

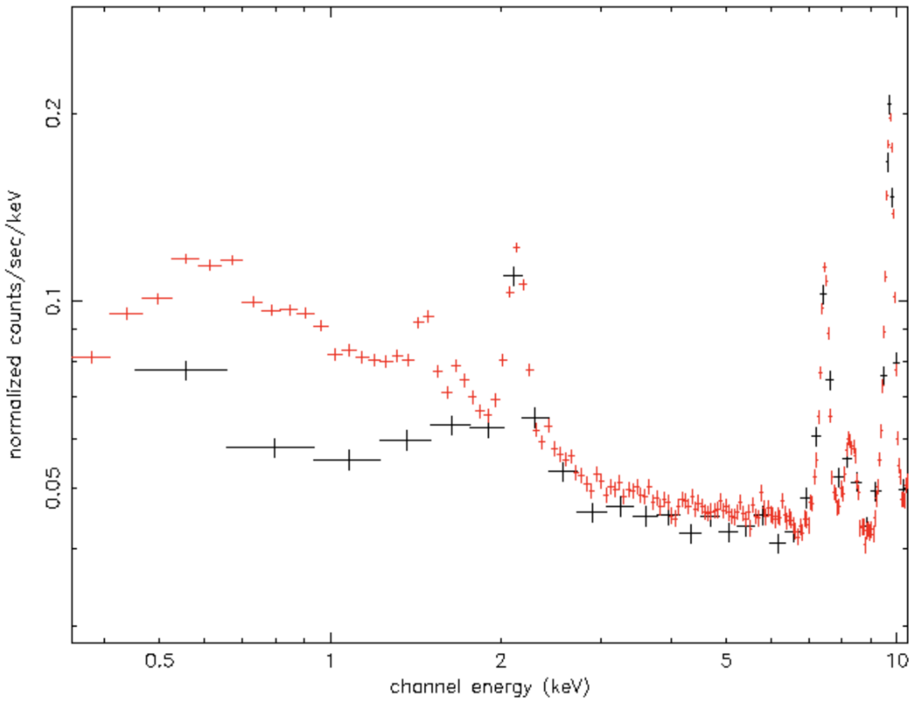

Figure 2.4 The comparison of the blank-sky background spectrum (red) and stowed background spectrum (black).[E08]

To remove the background component, we used stowed background images of ACIS-I chips. We first applied the `acis_process_events` routine to match the values of individual observations. Next, we reprojected the backgrounds so that their orientation matched each observation image using `reproject_events`.

As it is necessary to know the normalization factors, we separated the 9.5-12 keV interval from both the stowed backgrounds and from individual observations since, in this energy range, there is no actual signal in the dataset. Because only the noise is present, the count rate for individual observations is the same for background and observation. We then calculated the normalization factors as the ratio of total counts from observations and the backgrounds. Before the subtraction, we multiplied the stowed spectra by a normalization factor to match the observed values.

2.2.3 Data imaging

In order to get an overall Chandra Deep Field-South image of all the obtained observations, we used the `merge_obs` process. The final image can be seen in Figure 2.5. The command takes individual observations, reprojects them to a common reference frame and then merges them.

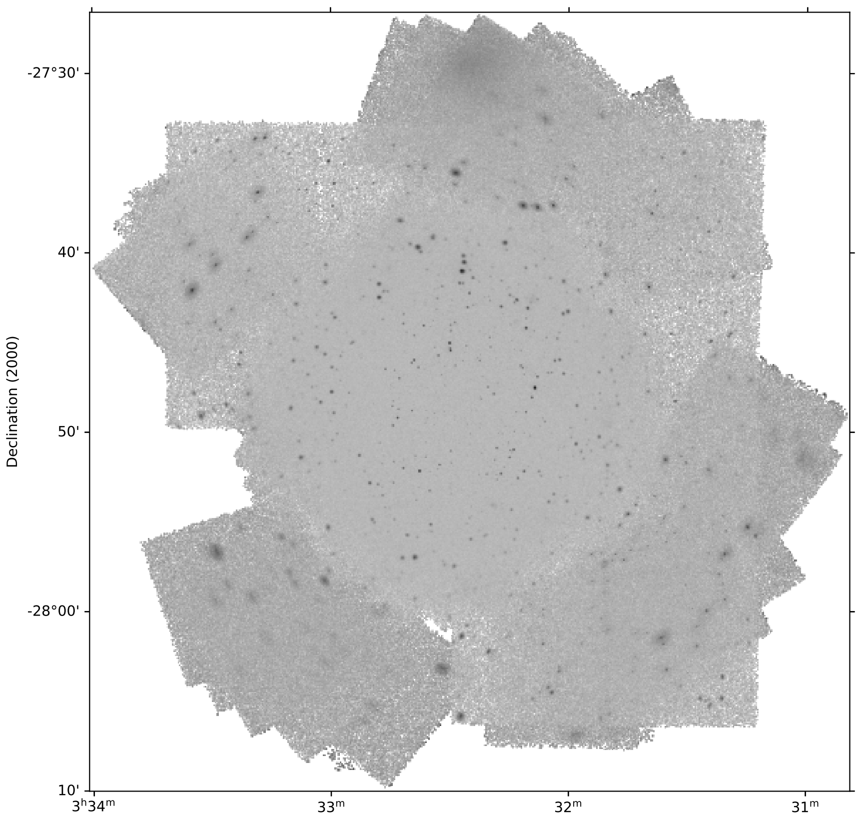

Figure 2.5 The Chandra Deep Field-South merged image from all used observations.

Next, it creates an overall exposure map to create an exposure-corrected image. The image created in this way does not show, for example, gaps between the chips or areas with weaker flux due to lower exposure. Note that such an image is heavily edited and, therefore, cannot be used for spectral analysis.

2.2.4 Point source exclusion

As the main focus of our work is the unresolved emission consisting of the diffuse emission, point sources need to be subtracted from our dataset before the spectral analysis. The source of point sources present in the CDFS image are mainly AGNs. Nevertheless, other contributions could also originate from star-forming galaxies or foreground stars. In the CDFS field of view, too many point sources are present to use `wavedetect` for source identification or to manually select the regions. Therefore catalogue by Luo et al. (2017) was used.

It is apparent from Figure 2.5 that despite the same theoretical size of the point sources (as they are delta functions), the proportions differ depending on the source position on the detector. This difference is caused by mirror aberrations on the telescope, and it can be described by the so-called point spread function (PSF). The overall area of the PSF depends on the source position as well as on the spectral energy distribution. In addition, the shape can also vary with the number of source photons. At around five arcminutes, regions enclosing the PSF start to overlap, as demonstrated in Figure 2.6. The minimum background area is then left, and therefore we use only five arcmin area around the Aimpoint in the spectral analysis.

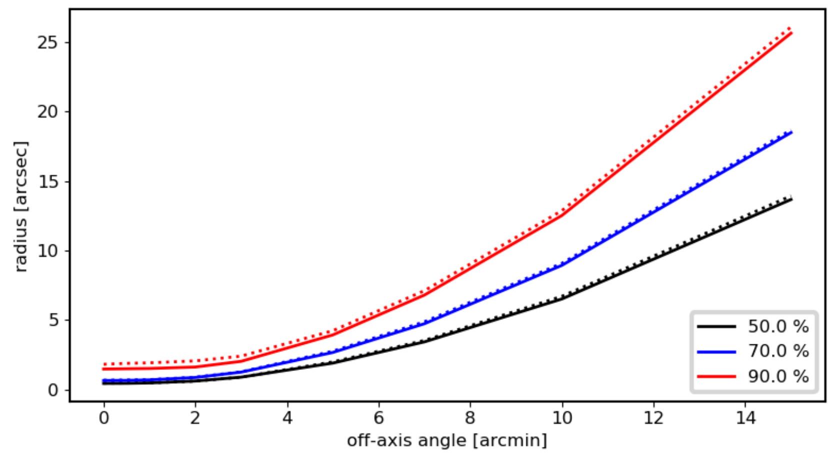

Figure 2.6 Simulated radius of encircled count fraction for different off-axis angles. [E09]

The coordinates from the Luo et al. (2017) catalogue were used as an input file in `psfsize_srcs` routine, which calculates the source region size based on its position on the CCD detector. The region size has been selected to enclose 98% of the point spread function at the 2.3 keV energy. Figure 2.7 shows the CDFS image with the used source regions.

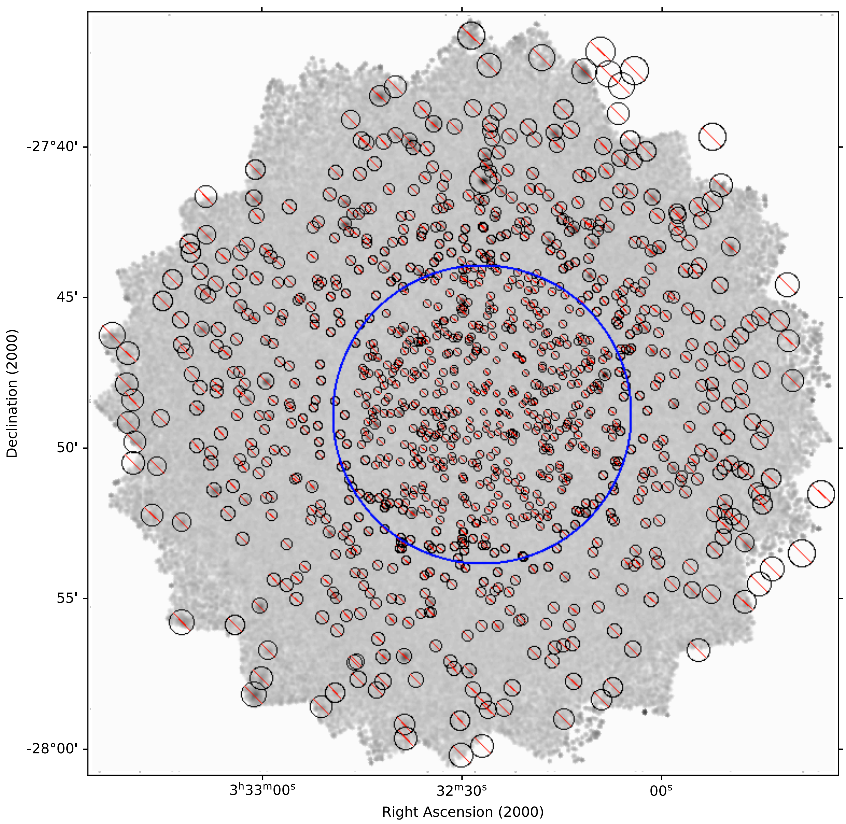

Figure 2.7 Chandra Deep Field-South image with selected point sources (black) from Luo et al. (2017) catalogue and 5 arcminute enclosing region (blue).

Chapter 3

Results

3.1 Spectral analysis

Over 100 observations of the Chandra Deep Field-South were analyzed. The spectra were extracted individually and combined year by year to understand the difference during a more extended period. For the final spectral analysis, we used only the observations from 2000, as the soft band's noise became significant afterwards. The quality of the fit was better only including these observations, as a contamination layer accumulated on the detector, leading to lower quality of the data in the soft band.

We used the spectral fitting package SPEX (Kaastra et al., 1996) for the analysis. The SPEX software package was designed to describe high-energy spectra, especially from current X-ray missions such as XMM-Newton, Chandra, Suzaku, or Hitomi. Several components were used in this analysis to describe obtained spectrum of the unresolved emission in the Chandra Deep Field-South.

3.1.1 Fitting spectra using Collisional Ionization Equilibrium model

The main contribution to the unresolved emission in the CDFS below 1 keV comes from the Galactic halo, then to a lesser extent a LHB, and 0.6 keV component. All of these elements consist of emitting plasma in collisional equilibrium. Therefore we used *Cie*: Collisional ionization equilibrium model to describe the thermal emission and determine spectral parameters.

Plasma in the collisional ionization equilibrium state often occurs in the Universe. We can observe it, for example, in the solar corona, in the stellar winds of hot stars, in hot plasma in the ISM and CGM, inside galaxy clusters, or in the cosmic web filaments. In this type of plasma, collisions with thermal electrons determine the production of X-rays. (Kaastra et al., 2017)

The *Cie* model calculates the spectrum based on two main steps, calculation of ionization balance and calculation of X-ray spectrum. Calculations use overall three temperatures. The most important being the electron temperature T_e. It determines the overall shape of the continuous spectrum and is equal to the plasma temperature that the model calculates via the fitting procedure.

Another temperature that the *Cie* model deals with is the temperature of ions T_i. This parameter appears only in high-resolution spectra and will determine the broadening of the spectral lines. The last temperature parameter is T_b, the so-called ionization balance temperature, which determines the plasma equilibrium state. By definition, the ratio of the electron temperature to the balance temperature is equal to one. If the ratio deviates from one, the plasma is no longer in equilibrium, and another model in the SPEX package would be used to describe plasma in a non-equilibrium state.

3.1.2 Fitting the Chandra Deep Field-South spectra

In addition to the *Cie* model, we included other components for computing the physical properties of the diffuse emission observed in the CDFS. Power law: *Pow* component took into account the unresolved point sources dominating the spectrum above 1 keV. To incorporate absorption by the ISM, *Abs*: the absorption model was used.

The complete model was set, so the ISM absorbed the thermal emission from the Galactic halo, 0.6 keV, and power law components. On the other hand, emission from the LHB was unabsorbed as it is located in the Earth's vicinity. The total model fitted is

$$Cie_{LHB} + (Cie_{GH} + Cie_{0.6} + pow) * abs. \tag{3.1}$$

The resulting spectrum can be seen in Figure 3.1.

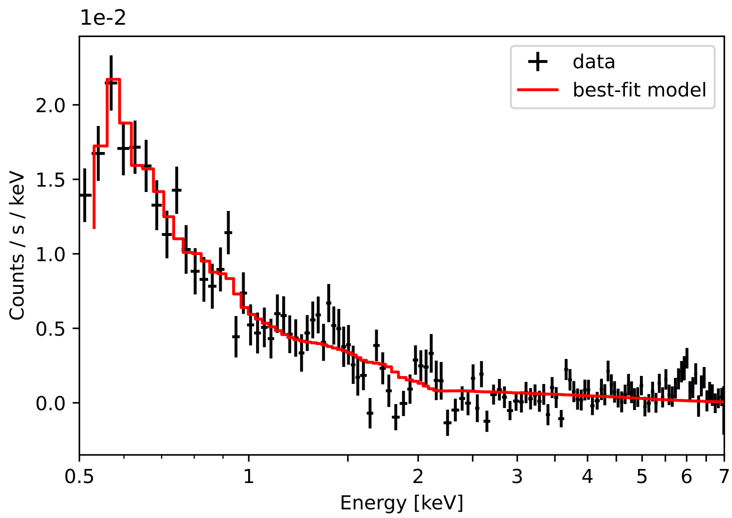

Figure 3.1 Spectrum of the CDFS (black) with best fit model (red).

The C-statistic was used for the fit evaluation. It is convenient to use C-statistics in the case of spectra with a small number of counts, where χ^2 cannot be considered. The maximum likelihood of the C-statistic is

$$C = -2 \ln \mathcal{L}_{poisson} + constant, \tag{3.2}$$

here $\mathcal{L}_{poisson}$ is the Poisson likelihood. The fit quality is assessed by the ratio of χ^2, calculated for the best model during C-statistic fitting, and degrees of freedom (dof).

The spectrum was fitted in the 0.5-7 keV energy range. The Chandra telescope is not sensitive below this band. On the other hand, above 7 keV, noise starts to overpower the actual signal. Together with residual spectral lines originating from the background present, they would lower the fit quality, therefore, the spectrum was cut at this value.

Firstly, we included a model with Galactic absorption. The absorbing column density was froze to $n_H = 7.02 \times 10^{19}$ cm^{-2} according to value from (Moretti et al., 2012). The power law component was also added to represent the unresolved point sources. The Γ parameter was set to initial value $\Gamma = 1.4$ and as free along with its normalization. Finally, we added only one thermal *Cie* component, representing Galactic halo emission. The parameter describing plasma temperature t and the normalization n were set free. This model was then fitted to the spectrum. The best-fit parameters can be seen in Table 3.1.

Table 3.1 The best-fit parameters for a model with only Galactic halo (GH) emission.

	t[keV]	n_t
GH	$0.146^{+0.002}_{-0.002}$	21^{+1}_{-1}

Γ	n_Γ
$1.66^{+0.13}_{-0.12}$	$1.49^{+0.19}_{-0.16}$

After the best fit for one temperature model was evaluated, another *Cie* model was added to consider LHB emission. This model is unabsorbed, and in agreement with the previous step, the parameters t and n were set free. Data were then fitted. The fit parameters can be seen in Table 3.2

Table 3.2 The best-fit parameters for a model with two temperatures included.

	t[keV]	n_t
GH	$0.146^{+0.003}_{-0.003}$	21^{+1}_{-2}
LHB	$7.25^{+7.25}_{-7.25} \times 10^{-2}$	2^{+2}_{-2}

Γ	n_Γ
$1.66^{+0.18}_{-0.17}$	$1.49^{+0.13}_{-0.12}$

Then the third *Cie* component was added to the model. This model is used to represent the 0.6 keV component. After fitting the data, the determined parameters can be seen in Table 3.3.

Table 3.3 The best-fit parameters for three temperatures model.

	t[keV]	n_t
GH	$0.148^{+0.004}_{-0.002}$	$21.7^{+1.1}_{-2.1}$
LHB	$6.45^{+6.45}_{-6.45} \times 10^{-2}$	$0.83^{+0.83}_{-0.83}$
0.6 keV	$0.514^{+0.514}_{-0.514}$	0^{+0}_{-0}

Γ	n_Γ
$1.66^{+0.19}_{-0.17}$	$1.49^{+0.13}_{-0.12}$

The goodness of the fit for all three variants can be seen in Table 3.4

Table 3.4 The goodness of the fit values for all three models.

	χ^2	dof	χ^2/dof
GH	276.32	252	1.097
GH+LHB	276.30	250	1.105
GH+LHB+0.6	276.30	248	1.114

Tables 3.1,3.2,3.3, and 3.4, suggest the first model best describes the spectrum with only one temperature included as the χ^2/dof is the lowest in this case. Although the goodness of the fit is similarly good in all three cases, the temperature t and normalization n were determined to have 100% error in both LHB and 0.6keV cases, suggesting that only Galactic halo thermal emission is significant in our dataset. However, in order to decide which model describes data the best, χ^2/dof may not be sufficient, therefore, further analysis is needed. We also tried the version where the LHB temperature is fixed at $kT = 0.097$ keV according to the value from Liu et al. (2017). However, normalization remained a free parameter. The fit quality changed little after this adjustment to $\chi^2/dof = 1.101$, but the normalization error remained 100%.

3.2 Model comparison using Bayesian analysis

A Bayesian analysis was created as an alternative for fitting spectra with a small number of counts. Using the Poisson likelihood to examine the parameter space makes it much more helpful for this dataset. The same method is applied when using other fitting methods, such as the C-statistic. Unlike in C-statistic, the parameter space is deformed by so-called priors. During the analysis, the variable is not taken as a fixed unknown value but as a random value that a probability function can describe. Markov Chain Monte Carlo (MCMC) can be used to calculate the parameters. This process takes an initial point and tests it against another point randomly drawn from a prior distribution. With a certain probability, this point is taken as a new starting point, and a parameter chain is created. Since MCMC has a few issues, for example, a problem may arise if two or more local maxima are present in the dataset, it is better to use Nested Sampling as an integration method. Thanks to this Monte Carlo method, points, called "live points", are always chosen randomly from the prior distribution. New points are then selected from the distribution. The process continues until a point with a higher likelihood is found. In this way, less likely points are gradually eliminated. MultiNest can be used to solve the dimensionality problem that may occur. The live points are stacked in multi-dimensional clusters. In these clusters, new points are selected, assuming that higher-valued points lie near the already selected points. This way, the integral from the parameter space is calculated globally and for each possible local maximum. (Buchner et al., 2014)

The Bayesian algorithm compares models, describing the spectrum, using integrals over parameter space.

$$Z = \int \pi(\vec{\Theta}) \exp\left[-\frac{1}{2}C(\vec{\Theta})\right] d\vec{\Theta}, \tag{3.3}$$

where $\vec{\Theta}$ is the parameter vector, $\pi(\vec{\Theta})$ is the weighting or deformation of the space by the prior, and C is the maximum likelihood of the C-statistics. Subsequently, the a priori expectation is compared with the Bayesian factor $B_{12} = Z_1/Z_2$. Information criteria, namely the Bayesian information criterion (BIC) and the Akaike Information Criterion (AIC), can also be used to compare the goodness of a model. Since BIC also considers the number of data points, and we fitted datasets with the same number of points, we will use AIC to compare the models. The AIC is described as

$$AIC = C - 2m. \tag{3.4}$$

The number of free parameters in the model is indicated by m. The smaller the AIC factor, the better the model is since the number of parameters in the model should be balanced with the likelihood, expressing the quality of the fit of the described model. (Buchner et al., 2014)

We used Bayesian analysis intending to compare the models describing the radiation from CDF-S, as comparing the quality of the fit may not be sufficient, especially when the χ^2/dof values are similar.

We performed a fit for a one-temperature, two-temperature, and three-temperature model. The free parameters correspond to the values obtained using the already performed fit from SPEX. Temperatures, photon index, and all normalizations were set as free parameters. Then a model comparison was made, and we calculated the AIC factor for all three models, as well as a $\log_{10}(Z)$ value. The results can be seen in Table 3.5.

Table 3.5 Bayesian analysis model comparison factors.

	AIC	$\log_{10}(Z)$
GH	659.2	-0.3
GH+LHB	657.7	0.0
GH+LHB+0.6	665.5	-4.3

We can see that the comparison results are very similar for all three models, confirming the findings from SPEX. Furthermore, the model with the lowest AIC factor is the most adequate, and they differ only by a small amount, indicating either the one-temperature or two-temperature model as the source of thermal emission because they are similar to each other in contrast to the three-temperature model. Here the determined $\log_{10}(Z)$ characterizes which description is more probable. The probability of the three-temperature model is $10^{4.3}$ times less likely than the two-temperature model and similarly, the probability of the one-temperature is $10^{0.3}$ times less likely.

We also have to consider the 100% errors in both added temperature parameters and their normalization. As in the previous step, we tested a model version with the LHB temperature set as constant with free normalization. This addition only slightly increased the probability of the two-temperature model from the previous 658.8 value to an AIC equal to 657.7. However, the normalization error remained 100%. The combination of parameter uncertainties and no significant improvement in the probability of a more complex model after the inclusion of an additional parameter points to the presence of only one temperature component.

Chapter 4

Discussion

We examined Chandra Deep Field-South spectra, measured by the Chandra telescope between 2000 and 2016. It is known that the diffuse emission consists of one extragalactic power law and three thermal components originating in our Galaxy. However, in the CDFS spectrum, we could confirm the existence of only one thermal source from the Galactic halo component.

Specifically, the soft part of the X-ray spectrum can be explained both by plasma radiation near the Sun called the Local Hot Bubble and by thermal emission from the CGM surrounding our Galaxy. It has also recently been confirmed that the Galactic halo emitting material at X-ray wavelengths is in a multi-temperature state. This confirms that this envelope has an extensive range of plasma states in different densities and temperatures. There is an ongoing complex system of material and energy exchange between the Galaxy and its outer part, mainly through supernova explosions but also thanks to the feedback of the SMBH in the Galactic center. However, there is also an opposite process where the matter in the Galactic halo falls back onto the Galactic disk and thus supports further star formation. The CGM thus plays a significant role in understanding the evolution of galaxies. Our results confirm the presence of only one thermal component with temperature $kT = 0.146 \pm 0.002$ keV. The temperature should be in the range of $kT \sim (0.15 - 0.20)$ keV. Our determined value is at the lower end of this interval, which can be explained by the fact that the CDFS region is a location with dimmer Galactic halo emission. Diffuse radiation from the halo is anisotropic, i.e. it is not the same in all positions. It also tends to be warmer in the vicinity of the Galactic disk, which is closer to the sources that heat the halo medium. On the contrary, CDFS is located near the Galactic pole and far from the disk.

As for radiation of extragalactic origin, the spectrum should follow the typical shape of the cosmic X-ray background with a photon index value of $\Gamma \sim 1.4$. Our determined value is $\Gamma = 1.66^{+0.13}_{-0.12}$. This value is slightly higher than the typical photon index for this type of radiation. We have to take into account that thermal emission also contributes to the overall photon index. Also, as shown in Hickox and Markevitch (2006), the photon index in the CDFS region tends to have higher values.

4.1 Observations of the soft X-ray diffuse emission

The most recent research on diffuse X-ray emission was done by Bluem et al. (2022) and Bhattacharyya et al. (2022). In these studies, the main focus was on the mystery 0.6 keV component. Bluem et al. (2022) used HaloSat all-sky survey to study the CGM of our Galaxy. According to them, the CGM is best described by two temperature phases. One warm component, which they calculated to be $kT = 0.166 \pm 0.005$ keV and one hot component, fitted as $kT = 0.69^{+0.04}_{-0.05}$ keV. Our measured value is lower than in the mentioned article. This fact can have many reasons. Firstly, in the paper, they analyzed the entire sky above the Galactic bulge and obtained the resulting temperatures by averaging all the measurements.

In comparison, our spectrum is a small portion of the entire sky, located near the South Pole. Furthermore, since the clumpy nature of both the warm and the hot components, CDFS may be located in a region with a lower temperature present. Bluem et al. (2022) also pointed out that when a model is split into more than one component, the temperature of the colder part is reduced. This could mean that, in our case, no other components than the one describing the cooler part of the hot Galactic halo are present. If the given elements were in the dataset, they would have merged into one one-temperature mode, and the model would have shown higher temperatures. On the contrary, in the case of multi-temperature models, the value representing the Galactic halo would have decreased, which did not happen.

XMM-Newton observations of CGM were performed and analyzed by Bhattacharyya et al. (2022). They performed analysis around the sightline of blazar Mrk 421. According to them, a two-phase model best describes the Galactic halo. The temperatures they found are $kT = 0.19^{+0.02}_{-0.01}$ keV and $kT = 0.66^{+0.12}_{-0.10}$ keV. These results also have higher values than our reported results, which is consistent with the considerations given above. These values also differ by a few hundredths from the outcome in Bluem et al. (2022).

All of the above findings indicate anisotropy in the structure and distribution of the CGM. Most likely, there is a large variability in the observed temperatures. There is also clustering of both the hot and cooler parts (even on smaller scales). The CGM could even have a filamentary structure as stated in Bhattacharyya et al. (2022). This clustering results in an environment of both various turbulences and outflows from the Galactic disk.

4.2 Comparison with older Chandra Deep Field observations

Determining the temperature in the CDFS has been the subject of studies in the past. The analysis of the Chandra Deep Fields was done by Hickox and Markevitch (2006). In their work, they presented a study of the unresolved X-ray emission in the CDFS and CDFN images in the 0.5-7.3 keV energy band. They used the XSPECs APEC plus power law model to describe X-ray emission from both Chandra deep fields. In the case of CDFS, from higher energies ($E > 1$ keV), the spectrum is described by power-law with photon index $\Gamma = 1.84^{+0.48}_{-0.35}$. On the other hand, they described soft X-ray spectrum as thermal with temperature $kT = 0.175^{+0.010}_{-0.019}$ keV.

Both the photon index and temperature value differ from our determined numbers. There can be many reasons behind it. The most probable scenario is that our data processing was different, as the CIAO pipelines changed over the years, to be more precise. Similarly, in the case of background subtraction, when our method varies from the procedure used in the paper mentioned above. We also used SPEX for the spectral fitting, which has different calculation processes than XSPEC. Moreover, as already mentioned in the text above, the most recently determined value of the temperature of diffuse X-ray radiation is cooler than expected. The reason behind the smaller photon index is evident as we used a more recent catalogue, and thus, we subtracted more point sources, resulting in a lower photon index.

Chapter 5

Summary and Conclusion

We analyzed a total of 109 Chandra Deep Field-South observations measured from 2000 to 2016. Background flares, as well as stowed backgrounds, have been removed from individual images. For obtaining the unresolved emission, the resolved point sources were excluded. After data processing, measurements from 2000 were used for spectral analysis. The final spectrum was analyzed in the SPEX fitting package. The data were fitted by three models with different temperature components and then compared using Bayesian analysis to determine whether single or multiple thermal emissions describe the spectrum.

The source of the unresolved emission in the Chandra Deep Field-South is the diffuse X-ray radiation consisting of soft and hard segments. The hard part of the spectrum is of extragalactic origin, composed of unresolved AGN. In comparison, the soft part can be described by a combination of thermal emission from the Galactic halo surrounding our Galaxy and from plasma radiating near the Sun, the LHB. It is clear that in the atmosphere of our Galaxy is plasma with an extensive range of temperatures and densities. These temperatures also reach outside the X-ray region. Since the material in the Sun's vicinity and beyond the boundaries of the Galactic disk is in the form of hot plasma, the ongoing mechanisms can be explained by the collisional ionized equilibrium. On the other hand, in the case of radiation of extragalactic origin, a power-law dependence can be used for the description.

Our goal was to find which model describes the acquired spectrum better, whether it is possible to say that the origin of the unresolved emission in the CDFS is an emitting plasma described by one temperature or if several thermal components characterize it. We fitted the spectrum with an absorbed power-law dependence model to account for the unresolved point sources. The one-temperature model contains a component describing the Galactic halo plasma with a temperature of $kT \sim 0.15$ keV, also absorbed by the material in the Galactic disk. An addition for the two-temperature model is the thermal emission created in the cavity near the Sun vicinity with $kT \sim 0.07$ keV. Finally, the model, including multiple phases of the CGM, is characterized an additionally absorbed $kT \sim 0.6$ keV temperature component. The resulting χ^2/dof ratios obtained from the SPEX fitting package are very similar for all three models, with the resulting fit most suggestive of the one-temperature model, proposing the single-temperature plasma as a source of the X-ray emission.

The data were also fitted using Bayesian analysis to better understand which model characterizes the spectrum, allowing us to compare models using the Akaike Information Criterion. The final AIC factors are lowest for two thermal components, where the AIC for one-temperature and two-temperature models are almost equal, and the three-temperature model slightly differs. From this evidence and the fact that the temperature and its normalization have a 100% error, we can conclude that it is very likely that the temperature representing the hot phase of the CGM is not present to a greater extent in the CDFS region. Regarding the distinction between the remaining two models, the AIC factors did not significantly increase the probability of the two-temperature model, even after fixing the value according to the literature, indicating that adding another parameter is not supported by the data. Similarly to the previous case, the temperature representing the LHB and its normalization have a 100% error. The source of the soft unresolved emission in CDFS is likely to be a combination of thermal radiation from the plasma in the LHB and the single-temperature plasma located in the Galactic halo. However, because the Chandra telescope is not sensitive in regions where the LHB emission has its maximum, this temperature cannot be determined in our dataset. Therefore, our spectrum is best described by power law describing extragalactic sources and by Galactic halo thermal emission with single temperature distribution.

Bibliography

[E01]. https://webbtelescope.org/glossary.

[E02]. https://www.mpe.mpg.de/7461761/news20200619.

[E03]. https://cxc.harvard.edu/proposer/POG/html/index.html.

[E04]. https://cxc.harvard.edu/proposer/POG/html/chap6.html#tth_chAp6.

[E05]. https://cxc.harvard.edu/proposer/POG/html/chap7.html#tth_chAp7.

[E06]. https://cxc.harvard.edu/ciao/why/aciscleanvf.html.

[E07]. https://cxc.cfa.harvard.edu/ciao/threads/flare/.

[E08]. https://cxc.harvard.edu/contrib/maxim/stowed.

[E09]. https://space.mit.edu/cxc/marx/tests/PSF.html.

Robert Antonucci. Unified models for active galactic nuclei and quasars. ARA&A, 31:473–521, January 1993. doi: 10.1146/annurev.aa.31.090193.002353.

Souradip Bhattacharyya, Sanskriti Das, Anjali Gupta, Smita Mathur, and Yair Krongold. The hot circumgalactic medium of the Milky-Way: new insights from XMM-Newton observations. *arXiv e-prints*, art. arXiv:2208.07863, August 2022.

J.A. Bittencourt. *Fundamentals of Plasma Physics.* Springer New York, 2013.

Jesse Bluem, Philip Kaaret, K. D. Kuntz, Keith M. Jahoda, Dimitra Koutroumpa, Edmund J. Hodges-Kluck, Chase A. Fuller, Daniel M. LaRocca, and Anna Zajczyk. Widespread Detection of Two Components in the Hot Circumgalactic Medium of the Milky Way. ApJ, 936(1):72, September 2022. doi: 10.3847/1538-4357/ac8662.

Sanchayeeta Borthakur, Timothy Heckman, Jason Tumlinson, Rongmon Bordoloi, Christopher Thom, Barbara Catinella, David Schiminovich, Romeel

Davé, Guinevere Kauffmann, Sean M. Moran, and Amelie Saintonge. Connection between the Circumgalactic Medium and the Interstellar Medium of Galaxies: Results from the COS-GASS Survey. ApJ, 813(1):46, November 2015. doi: 10.1088/0004-637X/813/1/46.

W. N. Brandt and D. M. Alexander. Cosmic X-ray surveys of distant active galaxies. The demographics, physics, and ecology of growing supermassive black holes. A&A Rev., 23:1, January 2015. doi: 10.1007/s00159-014-0081-z.

W. N. Brandt and G. Hasinger. Deep Extragalactic X-Ray Surveys. ARA&A, 43(1):827–859, September 2005. doi: 10.1146/annurev.astro.43.051804.102213.

J. Buchner, A. Georgakakis, K. Nandra, L. Hsu, C. Rangel, M. Brightman, A. Merloni, M. Salvato, J. Donley, and D. Kocevski. X-ray spectral modelling of the AGN obscuring region in the CDFS: Bayesian model selection and catalogue. A&A, 564:A125, April 2014. doi: 10.1051/0004-6361/201322971.

Michal Dovciak. *Radiation of Accretion Discs in Strong Gravity*. PhD thesis, November 2004.

Drummond B. Fielding, Stephanie Tonnesen, Daniel DeFelippis, Miao Li, Kung-Yi Su, Greg L. Bryan, Chang-Goo Kim, John C. Forbes, Rachel S. Somerville, Nicholas Battaglia, Evan E. Schneider, Yuan Li, Ena Choi, Christopher C. Hayward, and Lars Hernquist. First Results from SMAUG: Uncovering the Origin of the Multiphase Circumgalactic Medium with a Comparative Analysis of Idealized and Cosmological Simulations. ApJ, 903(1):32, November 2020. doi: 10.3847/1538-4357/abbc6d.

R. Fitzpatrick. *Plasma Physics: An Introduction (2nd ed.)*. 2022. doi: https://doi.org/10.1201/9781003268253.

Antonella Fruscione, Jonathan C. McDowell, Glenn E. Allen, Nancy S. Brickhouse, Douglas J. Burke, John E. Davis, Nick Durham, Martin Elvis, Elizabeth C. Galle, Daniel E. Harris, David P. Huenemoerder, John C. Houck, Bish Ishibashi, Margarita Karovska, Fabrizio Nicastro, Michael S. Noble, Michael A. Nowak, Frank A. Primini, Aneta Siemiginowska, Randall K. Smith, and Michael Wise. CIAO: Chandra's data analysis system. In David R. Silva and Rodger E. Doxsey, editors, *Society of Photo-Optical Instrumentation Engineers (SPIE) Conference Series*, volume 6270 of *Society of Photo-Optical Instrumentation Engineers (SPIE) Conference Series*, page 62701V, June 2006. doi: 10.1117/12.671760.

B. Fuchs, D. Breitschwerdt, M. A. de Avillez, C. Dettbarn, and C. Flynn. The search for the origin of the Local Bubble redivivus. MNRAS, 373(3):993–1003, December 2006. doi: 10.1111/j.1365-2966.2006.11044.x.

M. Galeazzi, A. Gupta, and E. Ursino. Evidence for the Missing Baryons in the Angular Correlation of the Diffuse X-Ray Background. ApJ, 695(2):1127–1131, April 2009. doi: 10.1088/0004-637X/695/2/1127.

David B. Henley and Robin L. Shelton. XMM-Newton and Suzaku X-Ray Shadowing Measurements of the Solar Wind Charge Exchange, Local Bubble, and Galactic Halo Emission. ApJ, 808(1):22, July 2015. doi: 10.1088/0004-637X/808/1/22.

Ryan C. Hickox and David M. Alexander. Obscured Active Galactic Nuclei. ARA&A, 56:625–671, September 2018. doi: 10.1146/annurev-astro-081817-051803.

Ryan C. Hickox and Maxim Markevitch. Absolute Measurement of the Unresolved Cosmic X-Ray Background in the 0.5-8 keV Band with Chandra. ApJ, 645(1): 95–114, July 2006. doi: 10.1086/504070.

J. S. Kaastra, R. Mewe, and H. Nieuwenhuijzen. SPEX: a new code for spectral analysis of X & UV spectra. In *UV and X-ray Spectroscopy of Astrophysical and Laboratory Plasmas*, pages 411–414, January 1996.

J. S. Kaastra, L. Gu, J. Mao, M. Mehdipour, F. Mernier, J. de Plaa, A. J. J. Raassen, and I. Urdampilleta. Science with hot astrophysical plasmas. *Journal of Instrumentation*, 12(8):C08008, August 2017. doi: 10.1088/1748-0221/12/08/C08008.

K. D. Kuntz. Solar wind charge exchange: an astrophysical nuisance. A&A Rev., 27(1):1, January 2019. doi: 10.1007/s00159-018-0114-0.

W. Liu, M. Chiao, M. R. Collier, T. Cravens, M. Galeazzi, D. Koutroumpa, K. D. Kuntz, R. Lallement, S. T. Lepri, D. McCammon, K. Morgan, F. S. Porter, S. L. Snowden, N. E. Thomas, Y. Uprety, E. Ursino, and B. M. Walsh. The Structure of the Local Hot Bubble. ApJ, 834(1):33, January 2017. doi: 10.3847/1538-4357/834/1/33.

Cassandra Lochhaas, Jason Tumlinson, Brian W. O'Shea, Molly S. Peeples, Britton D. Smith, Jessica K. Werk, Ramona Augustin, and Raymond C. Simons. Figuring Out Gas & Galaxies In Enzo (FOGGIE). V. The Virial Temperature Does Not Describe Gas in a Virialized Galaxy Halo. ApJ, 922 (2):121, December 2021. doi: 10.3847/1538-4357/ac2496.

Malcolm S. Longair. *High Energy Astrophysics.* 2011.

B. Luo, W. N. Brandt, Y. Q. Xue, B. Lehmer, D. M. Alexander, F. E. Bauer, F. Vito, G. Yang, A. R. Basu-Zych, A. Comastri, R. Gilli, Q. S. Gu, A. E. Hornschemeier, A. Koekemoer, T. Liu, V. Mainieri, M. Paolillo, P. Ranalli, P. Rosati, D. P. Schneider, O. Shemmer, I. Smail, M. Sun, P. Tozzi, C. Vignali, and J. X. Wang. The Chandra Deep Field-South Survey: 7 Ms Source Catalogs. ApJS, 228(1):2, January 2017. doi: 10.3847/1538-4365/228/1/2.

M. Markevitch, M. W. Bautz, B. Biller, Y. Butt, R. Edgar, T. Gaetz, G. Garmire, C. E. Grant, P. Green, M. Juda, P. P. Plucinsky, D. Schwartz, R. Smith,

A. Vikhlinin, S. Virani, B. J. Wargelin, and S. Wolk. Chandra Spectra of the Soft X-Ray Diffuse Background. ApJ, 583(1):70–84, January 2003. doi: 10.1086/345347.

A. Moretti, S. Vattakunnel, P. Tozzi, R. Salvaterra, P. Severgnini, D. Fugazza, F. Haardt, and R. Gilli. Spectrum of the unresolved cosmic X-ray background: what is unresolved 50 years after its discovery. A&A, 548:A87, December 2012. doi: 10.1051/0004-6361/201219921.

V. Pelgrims, K. Ferriere, F. Boulanger, R. Lallement, and L. Montier. Modeling the magnetized Local Bubble from dust data. A&A, 636:A17, April 2020. doi: 10.1051/0004-6361/201937157.

M. E. Putman, J. E. G. Peek, and M. R. Joung. Gaseous Galaxy Halos. ARA&A, 50:491–529, September 2012. doi: 10.1146/annurev-astro-081811-125612.

Stephan Rosswog and Marcus Brüggen. *Introduction to High-Energy Astrophysics*. 2007.

Peter Schneider. *Extragalactic Astronomy and Cosmology: An Introduction*. 2015. doi: 10.1007/978-3-642-54083-7.

Carl K. Seyfert. Nuclear Emission in Spiral Nebulae. ApJ, 97:28, January 1943. doi: 10.1086/144488.

M. Sharma, M. J. Page, and A. A. Breeveld. Galaxy luminosity functions at redshifts 0.6-1.2 in the Chandra Deep Field South. MNRAS, 511(4):4882–4899, April 2022. doi: 10.1093/mnras/stac356.

Jason Tumlinson, Molly S. Peeples, and Jessica K. Werk. The Circumgalactic Medium. ARA&A, 55(1):389–432, August 2017. doi: 10.1146/annurev-astro-091916-055240.

Catherine Zucker, Alyssa A. Goodman, João Alves, Shmuel Bialy, Michael Foley, Joshua S. Speagle, Josefa GroÎ²schedl, Douglas P. Finkbeiner, Andreas Burkert, Diana Khimey, and Cameren Swiggum. Star formation near the Sun is driven by expansion of the Local Bubble. Nature, 601(7893):334–337, January 2022. doi: 10.1038/s41586-021-04286-5.

All internet sources ([1] - [9]) were up to date 3.1.2023.